Monthly Notices
of the
ROYAL ASTRONOMICAL SOCIETY

MNRAS **476,** 3415–3424 (2018)
Advance Access publication 2018 February 19

doi:10.1093/mnras/sty414

Search for low-frequency diffuse radio emission around a shock in the massive galaxy cluster MACS J0744.9+3927

A. Wilber,[1⋆] M. Brüggen,[1⋆] A. Bonafede,[1,2] D. Rafferty,[1] F. Savini,[1] T. Shimwell,[3] R. J. van Weeren,[4] A. Botteon,[2,5] R. Cassano,[2] G. Brunetti,[2] F. De Gasperin,[4] D. Wittor,[1] M. Hoeft[6] and L. Birzan[1]

[1]*Hamburger Sternwarte, University of Hamburg, Gojenbergsweg 112, D-21029 Hamburg, Germany*
[2]*INAF/Istituto di Radioastronomia, Via P Gobetti 101, I-40129 Bologna, Italy*
[3]*ASTRON, the Netherlands Institute for Radio Astronomy, Postbus 2, NL-7990 AA Dwingeloo, the Netherlands*
[4]*Leiden Observatory, Leiden University, PO Box 9513, NL-2300 RA Leiden, the Netherlands*
[5]*Dipartimento di Fisica e Astronomia, Università di Bologna, via P. Gobetti 93/2, I-40129 Bologna, Italy*
[6]*Thüringer Landessternwarte, D-07778 Tautenburg, Germany*

Accepted 2018 February 13. Received 2018 February 9; in original form 2017 December 15

ABSTRACT

Merging galaxy clusters produce low-Mach-number shocks in the intracluster medium. These shocks can accelerate electrons to relativistic energies that are detectable at radio frequencies. MACS J0744.9+3927 is a massive [$M_{500} = (11.8 \pm 2.8) \times 10^{14}\,\mathrm{M}_{\odot}$], high-redshift ($z = 0.6976$) cluster where a Bullet-type merger is presumed to have taken place. Sunyaev–Zel'dovich maps from MUSTANG indicate that a shock, with Mach number $\mathcal{M} = 1.0$–2.9 and an extension of ∼200 kpc, sits near the centre of the cluster. The shock is also detected as a brightness and temperature discontinuity in X-ray observations. To search for diffuse radio emission associated with the merger, we have imaged the cluster with the LOw Frequency ARray (LOFAR) at 120–165 MHz. Our LOFAR radio images reveal previously undetected AGN emission, but do not show clear cluster-scale diffuse emission in the form of a radio relic nor a radio halo. The region of the shock is on the western edge of AGN lobe emission from the brightest cluster galaxy. Correlating the flux of known shock-induced radio relics versus their size, we find that the radio emission overlapping the shocked region in MACS J0744.9+3927 is likely of AGN origin. We argue against the presence of a relic caused by diffusive shock acceleration and suggest that the shock is too weak to accelerate electrons from the intracluster medium.

Key words: galaxies: clusters: general – galaxies: clusters: individual: MACS J0744.9+3927 – galaxies: clusters: intracluster medium – radio continuum: galaxies.

1 INTRODUCTION

1.1 Cluster mergers and shocks

Mergers between galaxy clusters produce large-scale, low-Mach-number ($\mathcal{M} \leq 4$–5) shock waves in the intracluster medium (ICM). These shocks are thought to accelerate ICM particles to ultra-relativistic energies and potentially amplify ICM magnetic fields (e.g. Vazza, Brunetti & Gheller 2009; Brüggen et al. 2012; Vazza et al. 2017). Observations of merging clusters over a wide range of wavelengths are currently constraining the physics behind these shocks. See Hoeft & Brüggen (2007) and Brunetti & Jones (2014) for reviews of shocks and non-thermal emission associated with these events.

The thermal component of the ICM consists of hot gas (10^{7-8} K or 1–10 keV) that is visible in X-rays through bremsstrahlung emission. A merging cluster may show an elongated or disturbed X-ray morphology, usually indicating the direction of the merger. Shocks are pressure discontinuities that can be identified as sharp edges in the brightness and temperature distribution of the ICM X-ray emission (e.g. Markevitch et al. 2002; Markevitch & Vikhlinin 2007; Ogrean et al. 2013; Botteon, Gastaldello & Brunetti 2018).

The mass and merging status of a cluster can also be inferred from the thermal Sunyaev–Zel'dovich (SZ) effect, where electrons in the ICM upscatter cosmic microwave background (CMB) photons. The SZ decrement[1] is proportional to the line-of-sight integral of the plasma pressure and hence shocks appear as substructures in

⋆E-mail: amanda.wilber@hs.uni-hamburg.de (AW); mbrueggen@hs.uni-hamburg.de (MB)

[1] A decrement is seen only below ∼ 220 GHz; above this frequency there is an increment.

the SZ signal of a cluster. Since the SZ decrement has no dependence on the distance, there is the opportunity to discover shocks even in distant clusters (Komatsu et al. 2001; Kitayama et al. 2004; Mason et al. 2010; Korngut et al. 2011; Romero et al. 2015; Young et al. 2015). Ferrari et al. (2011) were the first to use MUSTANG SZ maps and X-ray data to confirm a shocked region in the most X-ray luminous cluster RX J1347−1145, and showed that there was a radio excess coincident with the shock in the form of a mini-halo. Recently, the SZ effect was used to characterize a shock in the Coma cluster using *Planck* data (Erler et al. 2015). More recently, Atacama Large Millimeter Array (ALMA) has achieved very high resolutions (up to 3.5 arcsec), detecting the highest redshift shock known ($z = 0.87$) in ACT-CL J0102−4915 or the 'El Gordo' cluster (Basu et al. 2016).

Many merging cluster systems are observed to host cluster-scale radio emission in the form of radio haloes and/or radio relics (see Feretti et al. 2012, for a review). Radio haloes are classified as diffuse emission at the cluster centre, thought to be the product of turbulent re-acceleration of ICM particles driven by a cluster merger (e.g. Brunetti et al. 2001). Gischt relics are classified as elongated or arching diffuse radio emission typically found on the cluster periphery (e.g. Rottgering et al. 1997; Bagchi et al. 2006; Bonafede et al. 2009, 2014; van Weeren et al. 2010, 2012), and are thought to trace shock waves induced by cluster mergers (Brüggen, van Weeren & Röttgering 2011; Brüggen et al. 2012). Active galactic nuclei (AGN) relics, or phoenix relics, are usually much smaller, more roundish in appearance, and consist of aged or 'ghost' AGN emission that has been re-energized by shocks (e.g Enßlin & Gopal-Krishna 2001; Slee et al. 2001; de Gasperin et al. 2015).

The details of the necessary acceleration mechanisms and the efficiencies of low-Mach-number shocks are still largely unknown (see Brunetti & Jones 2014, for a review). Along a shock front, diffusive shock acceleration (DSA) is believed to accelerate electrons that could produce synchrotron emission at radio wavelengths (Blandford & Ostriker 1978; Ensslin et al. 1998). However, the low Mach numbers of most observed shocks are usually too weak to accelerate particles from the thermal pool (Botteon et al. 2016a; Eckert et al. 2016; van Weeren et al. 2016b). Hence, some form of pre-acceleration or an upstream population of relativistic seed electrons is required for DSA to operate. One possible pre-acceleration mechanism is shock drift acceleration (Matsukiyo et al. 2011; Guo, Sironi & Narayan 2014a,b), which has been simulated in a cosmological context by Vazza et al. (2016) and Wittor, Vazza & Brüggen (2017). AGN are another potential source for seed electrons, and several examples have been found, the clearest being the connection between a radio relic and radio galaxy in Abell 3411-3412 (van Weeren et al. 2017).

Most merging clusters with X-ray detected shocks are shown to host some type of diffuse radio emission. There are a few cases where shocks coincide with the edges of radio haloes (e.g Markevitch et al. 2005; Uchida et al. 2016), but most shocks in merging clusters are associated with radio relics. Very recently, Hlavacek-Larrondo et al. (2018) presented highly sensitive Jansky Very Large Array (VLA) observations of the low-mass merging cluster Abell 2146 that revealed diffuse radio emission associated with two confirmed X-ray shocks, which was previously undetected by Russell et al. (2011) in observations by the Giant Metrewave Radio Telescope (GMRT).

Searching for diffuse radio emission at confirmed shock locations in the ICM is a key test to validate the widely held model that radio relics are produced by shocks. Radio observations of smaller shocks and shocks with lower Mach numbers are especially of interest, potentially yielding limits on the efficiencies of theorized acceleration mechanisms. High-redshift clusters also test the sensitivities of our radio telescopes, and allow us to determine the effect of inverse Compton scattering, which becomes stronger as the CMB energy density increases.

1.2 MACS J0744.9+3927

An intracluster shock sits just outside the centre of the massive and distant galaxy cluster MACS J0744.9+3927 (Korngut et al. 2011). This cluster is located at RA: $07^{h}44^{m}52\overset{s}{.}47$, Dec.: $+39^{\circ}27'27\overset{''}{.}3$, at a redshift of $z = 0.6976$ (Ebeling et al. 2007). Durret et al. (2016) give a mass derived from the *XMM–Newton* archival data as $M_{500} = 9.9 \times 10^{14}\,M_{\odot}$. MACS J0744.9+3927 is a CLASH (Cluster Lensing And Supernova survey with Hubble; Postman et al. 2012) cluster with a weak lensing derived mass of $M_{500} = (11.837 \pm 2.786) \times 10^{14}\,M_{\odot}$ (Sereno et al. 2015), consistent (within 1σ) with the *XMM*-derived mass.

Using MUSTANG observations, Korngut et al. (2011) found an SZ decrement as a kidney-shaped ridge in the north–south direction with a length of ∼25 arcsec (180 kpc). The kidney-shaped feature is located between the system's main mass peak and a second, smaller mass peak. The region of this ridge overlaps a discontinuity in the *Chandra* X-ray image. To accurately quantify the discontinuity, Korngut et al. (2011) measured X-ray surface brightness and temperature changes over the elliptical radius of the cluster, and found that there is temperature increase and a slight brightness drop-off coincident with the SZ decrement, suggesting that this region is shock-heated gas and the second highest redshift shock known after the one in El Gordo (Botteon et al. 2016b).

The Mach number obtained from the density jump conditions, as calculated from the fit to the X-ray surface brightness, was $\mathcal{M} = 1.2^{+0.2}_{-0.2}$ where the errors are 1σ. The temperature jump conditions at the shock yield a higher value, $\mathcal{M} = 2.1^{+0.8}_{-0.5}$; however, the error bars are large and the value agrees with the Mach number inferred from the density jump condition at the 1.3σ level. The shock velocity in this cluster is $V_{\rm sh} = 1827^{+267}_{-195}\,{\rm km\,s^{-1}}$ assuming the Mach number obtained from the density jump conditions (Korngut et al. 2011).

The dynamics of the cluster–subcluster merger is unclear. A subcluster lies 300 kpc west of the centre of the main cluster, and a mass lensing reconstruction from Richard et al. (2011) shows elongation towards the west. Korngut et al. (2011) suggest that the subcluster has passed through the main cluster core from the east to the west in a Bullet-type fashion and ram pressure has stripped off baryons from the subcluster. Shocked gas appears to be hugging the westward portion of the main cluster core, in between the two merging clusters, which is not the place where a merger shock would be expected. Typically, the shocks found in Bullet-type mergers, either bow or counter, are found outside the merged system as a whole, and not in between the two subclusters (e.g Russell et al. 2010; Shimwell et al. 2014; Botteon et al. 2016b). The size and position of the shock suggest that it is not the type of merger shock that has been observed to produce prominent radio relics such as the Sausage (e.g. Hoang et al. 2017) or Toothbrush (e.g. van Weeren et al. 2016b) relics because those are all on the peripheral regions of the cluster and exhibit significant scale (∼1 Mpc). Guennou et al. (2014) presented an X-ray image of the cluster from *XMM–Newton* and state that the residual X-ray image shows an extended structure coincident with the SZ excess as seen by Korngut et al. (2011), but they favour the scenario that the extended appearance is due to a substructure attached to the cluster, potentially from an infalling group. The direction of the potential infalling group and the angular separation between it and the main cluster are uncertain.

Radio surveys covering MACS J0744.9+3927, including the Faint Images of the Radio Sky at Twenty-Centimeters (White et al. 1997) and the NRAO VLA Sky Survey (Condon et al. 1998), do not detect any significant radio sources in the cluster field. MACS J0744.9+3927 was selected to be targeted with the LOw Frequency ARray (LOFAR; van Haarlem et al. 2013) because it is a very-high-mass and high-z cluster with evidence of merging activity and a shock detection in SZ. In this paper, we present LOFAR observations of MACS J0744.9+3927 at 120–165 MHz (with a central frequency of 143 MHz) to search for a radio relic associated with the shock. LOFAR's sensitivity to steep-spectrum low-surface-brightness emission is crucial for detecting weak and diffuse radio emission on cluster scales. Assuming the following cosmology, $H_0 = 70$, $\Omega_m = 0.3$, and $\Omega_\Lambda = 0.7$, the angular scale at MACS J0744.9+3927's redshift ($z = 0.6976$) is 7.223 kpc arcsec^{-1}, used hereafter.

2 LOFAR OBSERVATION OF MACS J0744.9+3927

LOFAR is a low-frequency radio interferometer with a compact core and stations that extend over large parts of Northern Europe (van Haarlem et al. 2013). Our observation was part of the LOFAR Two-metre Sky Survey (LoTSS; Shimwell et al. 2017) and uses the high-band antennas over a frequency range of 120–165 MHz. The data reduction steps for these data are identical to the data reduction steps described in Wilber et al. (2018), and are summarized below.

2.1 PREFACTOR

PREFACTOR[2] is a package containing automated pipelines called Pre-Facet Calibration and Initial Subtract. Pre-Facet Calibration compresses and averages the original data and performs all initial, direction-independent calibration. In this step, a flux calibrator (observed at the beginning and end of the target observation) is used to compute amplitude gain solutions, station clock offsets, station phase offsets, and station differential total electron content (TEC). Amplitude gain solutions and corrections for clock and phase offsets are then transferred to the target field data. An initial phase calibration is also performed using a global sky model from the TIFR GMRT Sky Survey (TGSS) at 150 MHz (Intema et al. 2017). For this observation, the calibrator 3C196 was used, a bright quasar [66 Jy at 159 MHz according to the Scaife & Heald (2012) absolute flux scale]. After the direction-independent calibration is completed, preliminary imaging is carried out via the Initial Subtract pipeline. The full wide field of the calibrated target data is imaged in high and low resolution using `WSClean` (Offringa et al. 2014). These full field images are used to model and subtract all sources in preparation for direction-dependent calibration.

2.2 FACTOR

Direction-dependent calibration for LoTSS data is significantly simplified and refined through the facet calibration technique (van Weeren et al. 2016a). This method of calibration is executed via the FACTOR[3] software package. FACTOR first tessellates the full target field into several smaller patches of sky called facets. Each facet is automatically chosen to be centred on a bright compact source to be used as a facet calibrator. TEC, phase, and amplitude solutions are computed from the facet calibrator and applied to all sources in that facet. Facets are processed in order of brightness and as the brighter sources are progressively subtracted, with adequate calibration solutions, the effective noise in the uv-data is reduced. After a facet is calibrated, it is imaged with `WSClean` and a primary beam correction is applied. For more details on facet calibration, the reader is referred to van Weeren et al. (2016a) and Williams et al. (2016).

For this observation, FACTOR was run on the full 45 MHz bandwidth of target data. The wide field was tessellated into 40 directions with one direction designated as the target facet, containing MACS J0744.9+3927, and 18 bright and nearby facets were processed before imaging the target facet. The target facet was imaged after applying the calibration solutions from a nearby[4] bright source in a neighbouring facet. The final image of the target facet produced by FACTOR has a resolution of 8.6 arcsec × 6.5 arcsec with root mean square (*8rms) noise of $\sigma \approx 180\,\mu$Jy beam^{-1}.

Data calibrated with FACTOR often show a slight astrometric offset because phase solutions change quickly over small regions of sky (due to the spatially changing conditions of the ionosphere; Williams et al. 2016). The LOFAR map was initially offset from the optical and SZ map. We calculated an astrometric shift by comparing the LOFAR radio map at 143 MHz to a high-resolution GMRT map at 610 MHz with corrected astrometry from van Weeren, Intema & Lal (in preparation). We measured the offset in arcseconds between the maximum pixel locations of several point sources in and around the cluster centre. A shift of RA, Dec.: [−2.5,0] arcsec was applied to all LOFAR images to match the GMRT astrometry.

3 RESULTS

3.1 Subtraction of compact sources

Our LOFAR image of MACS J0744.9+3927 shows an active galaxy at the cluster centre. It sits within the X-ray emission of the cluster but slightly towards the east (see Fig. 1). This central AGN is likely associated with the optical source SDSS J074452.77+392726.7, the brightest cluster galaxy (BCG), with a redshift of $z = 0.6986 \pm 0.0007$.[5] The radio emission from this galaxy appears round and compact in the high-resolution image. There is another compact radio source on the northern edge of the X-ray emission (labelled in Fig. 1). This emission might come from an active galaxy, but the only optically visible galaxy coincident with the radio peak in this region does not have a confirmed redshift (SDSS J074452.36+392748.8). Therefore, it is not possible to say whether this northern emission is a background or foreground galaxy, or if it is actually extended lobe emission from the AGN associated with the BCG.

In order to search for cluster-scale diffuse emission associated with the shocked region, a subtraction of compact sources was carried out using CASA (Common Astronomy Software Applications; McMullin et al. 2007). The subtraction was performed on the uv-data by imaging with a uv-range of $> 6000\,\lambda$ (filtering out emission that spans more than 34 arcsec or ~ 250 kpc)[6] and Briggs' robust

[2] https://github.com/lofar-astron/prefactor
[3] http://www.astron.nl/citt/facet-doc/

[4] $\sim 0.^\circ 3$ angular separation.
[5] From the Sloan Digital Sky Survey Data Release 1 as obtained on 2003 August 28 from http://das.sdss.org/DR1/data/spectro/ss_tar_20/
[6] We also attempted the subtraction at a uv-range of $> 2000\,\lambda$ and $> 4000\,\lambda$, which correspond to emission spanning less than ∼750 kpc and ∼400 kpc, respectively, but decided to increase the cut to reduce the possibility of

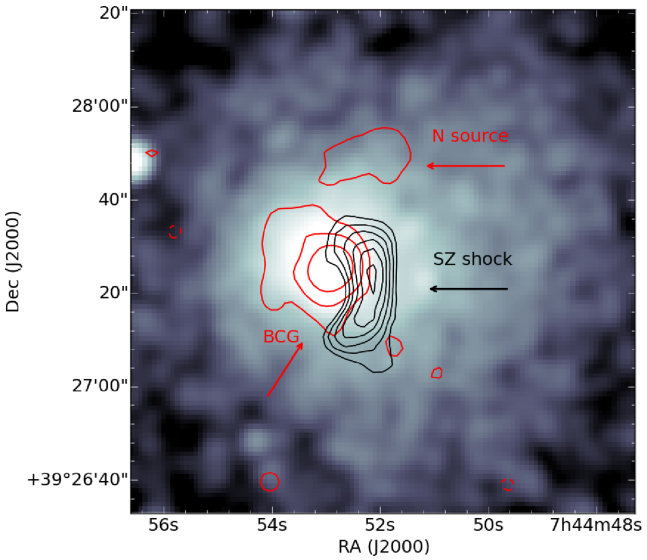

Figure 1. *Chandra* X-ray emission in blue with LOFAR high-resolution FACTOR image contours $[-3, 3, 6, 12] \times \sigma$ overlaid in red. X-ray emission is smoothed with a Gaussian kernel. rms noise of our LOFAR image is $\sigma = 180$ μJy beam^{-1} with a beam size of 8.6 arcsec × 6.5 arcsec. Black contours show the SZ decrement as detected by MUSTANG, from Korngut et al. 2011, starting at 3σ with 0.5σ increments. LOFAR detects a compact BCG AGN and a compact northern source.

parameter of 0.25. The CLEAN components of the resulting image were then subtracted from the uv-data set using the tasks FTW and UVSUB. The data set was then re-imaged with a uv-range of > 80 λ,[7] a slight outer uv-taper to bring out extended emission (6 arcsec as shown in Fig. 2 and 10 arcsec as shown in Fig. 3),[8] and a robust parameter of 0. This method of compact source subtraction is not perfect and the resulting image may still include residual emission or artefacts associated with the compact source, or diffuse emission can be subtracted, but a manual inspection of the CLEAN component model proved that no diffuse emission was removed.

Our final compact-source-subtracted image shows faint diffuse emission near the cluster centre extending to the north and south of the BCG (Figs 2 and 3). An optical image of the cluster with LOFAR compact emission and diffuse emission overlaid as contours can be seen in Fig. 4. The northern diffuse emission is brightest with a peak flux of 933 μJy within the 9σ contour where $\sigma = 200$ μJy beam^{-1} (in Fig. 3), which is likely from a separate AGN north of the BCG. We suspect that the diffuse emission at the cluster centre extending south-west is part of radio lobes associated with the BCG. There is no significant emission coincident with the kidney-shaped ridge seen in the SZ map. In fact, the diffuse radio emission falls off in the direction that the SZ decrement increases (see Fig. 4). There is also no diffuse emission resembling a radio halo at the cluster centre.

subtracting diffuse emission possibly related to the shocked region since this region is on a relatively small scale.

[7] FACTOR calibration solutions are determined from data with a uv-range of > 80 λ to eliminate the shortest baselines that can introduce significant large-scale emission manifested as noise. Since the target data are calibrated with solutions > 80 λ, we also image selecting data > 80 λ.

[8] Outer uv-taper values greater than 10 arcsec appeared to artificially inflate the size of existing emission due to smearing from a larger synthesized beam. Since it is at such high redshift, this cluster requires higher resolution imaging.

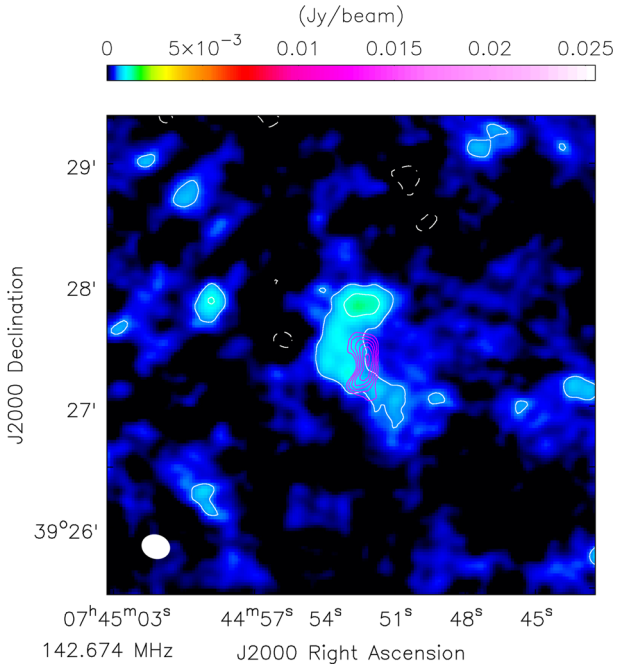

Figure 2. LOFAR image after subtracting compact sources imaged at a uv-range of > 6000 λ. An outer uv-taper of 6 arcsec was used to bring out diffuse emission. rms noise is $\sigma = 180$ μJy beam^{-1} and the restoring beam is 14 arcsec × 12 arcsec. White contours are $[-3, 3, 6, 9] \times \sigma$. Magenta contours show the SZ feature, considered to be a merger-induced shock, as detected by MUSTANG from Korngut et al. (2011).

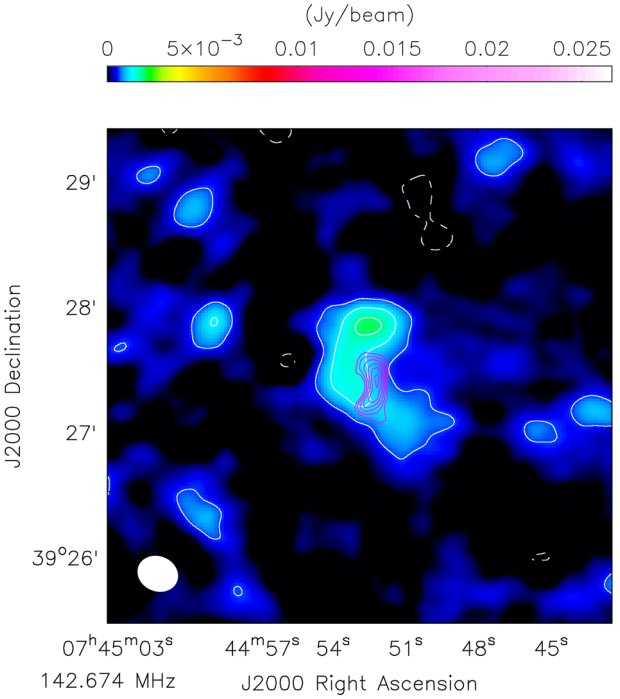

Figure 3. LOFAR image after subtracting compact sources imaged at a uv-range of > 6000 λ. An outer uv-taper of 10 arcsec was used to bring out diffuse emission. White contours are $[-3, 3, 6, 9] \times \sigma$, where $\sigma = 200$ μJy beam^{-1} and the restoring beam is 19 arcsec × 16 arcsec. Magenta contours are from the MUSTANG SZ map. Extended emission is visible up to 570 kpc, and likely consists of emission from multiple AGN.

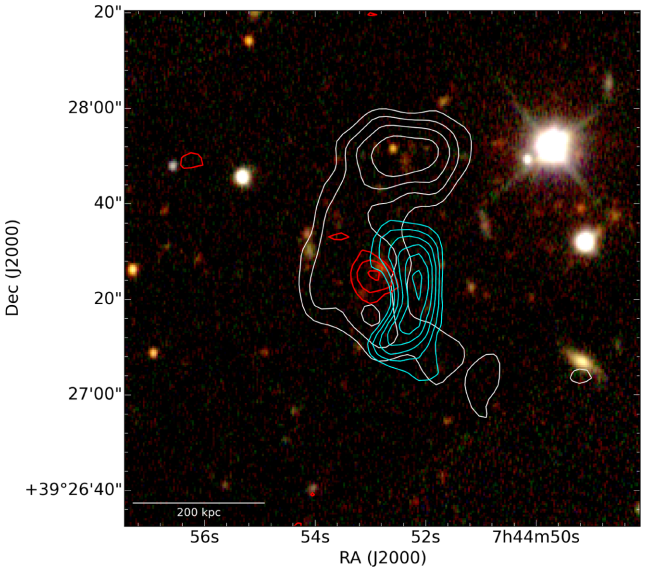

Figure 4. SDSS *g,r,i* image with radio emission overlaid as contours. LOFAR compact emission imaged with a uv-range $> 6000\ \lambda$ is shown by red contours [3, 6, 9] $\times\ \sigma$, where $\sigma = 200\ \mu$Jy beam^{-1}. LOFAR diffuse emission after compact source subtraction is shown in white contours where contours are [3, 4, 5, 6] $\times\ \sigma$ and $\sigma = 200\ \mu$Jy beam^{-1} (same as Fig. 3). Cyan contours are from the SZ MUSTANG map from Korngut et al. (2011).

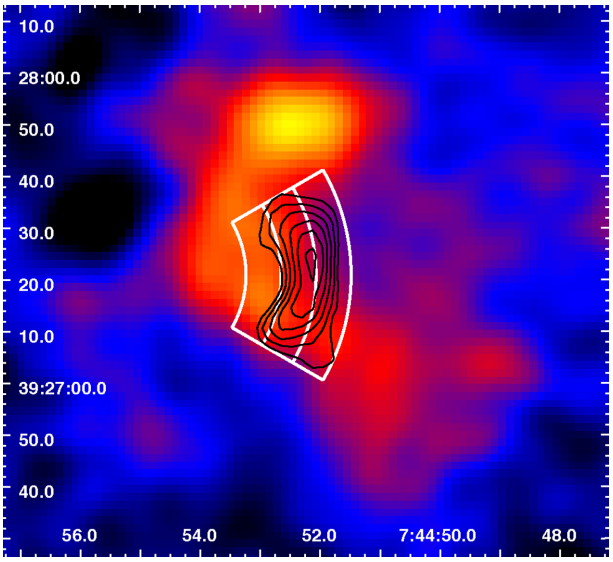

Figure 5. Pie cut region (shown in white) in which the flux density is measured to determine a radio relic upper limit. Black contours are from the MUSTANG map. The radio relic upper limit is measured from our compact-source-subtracted LOFAR image with an outer uv-taper of 6 arcsec.

3.2 Search for radio relics

There is no clear radio structure coinciding with the shock detected by Sunyaev-Zel'dovich effect (SZE) observations. The only emission present at the shocked region is what we suspect to be the fading south-western edge of the AGN lobe associated with the BCG. To determine an upper limit on a potential radio relic associated with the shock, we calculate the radio power within the shocked region from our low-resolution image (14 arcsec $\times$ 12 arcsec) made with the compact-source-subtracted uv-data set that was imaged in CASA CLEAN with an outer uv-taper of 6 arcsec (Fig. 2).

The flux density at 143 MHz is measured within a pie cut of three annuli, where the beginning and ending angles of the pie align with the north and south boundaries of the lowest contour (3σ) of the SZ decrement as seen by MUSTANG (presented in Korngut et al. 2011). Fig. 5 shows the pie cut annuli region in white and the SZ ridge in black overlaid on our low-resolution LOFAR image. The outer two annuli effectively cover the area of the shock as indicated by SZE observations, and the inner annulus extends from the inner edge of the kidney-shaped ridge towards the cluster centre.[9]

Within a region defined by the outer two annuli shown in Fig. 5, the flux density at 143 MHz is $S_{143} = 1.18 \pm 0.12$ mJy with a corresponding radio power of $P_{143} = (2.84 \pm 0.28) \times 10^{24}$ W Hz^{-1}. Within a region defined by the total pie cut, including the inner annulus, the flux density is found to be $S_{143} = 2.05 \pm 0.21$ mJy with a corresponding radio power of $P_{143} = (4.90 \pm 0.49) \times 10^{24}$ W Hz^{-1}. Here we include a k-correction to account for redshift using a spectral index of $\alpha = -1.2$ where $S \propto \nu^{\alpha}$. The error in our flux density measurement is assumed to be 10 per cent, which is determined by comparing flux densities of several sources in our LOFAR map to the same sources in TGSS (Intema et al. 2017) and the 7C survey (Hales et al. 2007).

We extrapolate the flux density value within the total pie cut, defined by the three annuli, to 1.4 GHz by assuming a range of potential spectral indices that include the typical values measured for relics found at merger shocks (gischt-type relics) and AGN relics, which can have even steeper spectral indices. We choose a conservative range of $\alpha = -1$ to -1.5. This gives a 1.4 GHz flux density range of $S_{1.4} = (0.06\text{–}0.23)$ mJy, corresponding to a radio power range of $P_{1.4} = (1.71\text{–}4.99) \times 10^{23}$ W Hz^{-1}.

In the above calculations for flux density and radio power at 1.4 GHz, we choose to use the 143 MHz flux density within the total pie cut (which is a region starting at the cluster centre and ending at the outer edge of kidney-shaped ridge, $\sim$140 kpc in width) rather than just using the flux that is coincident with the MUSTANG SZE contours. An ALMA detection from Basu et al. (2016) showed that a pressure discontinuity (SZ decrement) of the merger shock in El Gordo is coincident with the width of the radio relic seen at 2.1 GHz. However, MUSTANG has a lower resolution and lower sensitivity than ALMA, and radio relics are seen to widen at low frequencies. For this reason, we calculate the potential relic flux density from annuli covering the shocked region as indicated by SZE observations in addition to the flux within an annulus extending east of the SZ ridge towards the cluster centre.

In Table 1, we make a list of observed relics/candidate relics that are smaller [largest linear scale (LLS) <0.7 Mpc] and/or fainter ($\log_{10}(P_{1.4}) < 24.3$ W Hz^{-1})[10] than most gischt relics. In Fig. 6, we plot a large sample of observed radio relics by their power at 1.4 GHz versus their LLS. This sample is taken from a list of confirmed gischt-type relics and smaller phoenix relics presented in Nuza et al. (2017) as well as the additional smaller relics/candidate relics listed in Table 1. We calculate the power for each relic from the flux density at 1.4 GHz and include a k-correction with an average spectral index of $\alpha = -1.2$, as is used in Nuza et al. (2017). We include the extrapolated radio power range for the shocked region in MACS J0744.9+3927, using the LLS of the shock as seen

[9] The cluster centre as marked by the brightness distribution in X-ray emission.

[10] We note that the small relic in MAXBCG138+25 is perhaps an important outlier since it is much brighter than other small phoenix/AGN relics.

Table 1. Small and faint radio relics/candidate radio relics.

Relic	$\log_{10}(P_{1.4})$ (W Hz^{-1})	LLS (Mpc)	References
A13	23.85	0.25	Feretti et al. (2012), Slee et al. (2001)
A85	23.50	0.35	Feretti et al. (2012), Slee et al. (2001)
A725	23.11	0.44	Böhringer et al. (2000), Kempner & Sarazin (2001)
A2034 F	22.60	0.6	Shimwell et al. (2016)
A2048	23.66	0.31	van Weeren et al. (2011b)
A2443	23.30	0.43	Feretti et al. (2012), Cohen & Clarke (2011)
A4038	23.01	0.13	Feretti et al. (2012), Slee et al. (2001)
MAXBCG138+25	25.01	0.19	van Weeren, Röttgering & Brüggen (2011a)
Sausage R1	24.03	0.63	Hoang et al. (2017)
Sausage R2	24.27	0.67	Hoang et al. (2017)
Toothbrush D	24.15	0.25	van Weeren et al. (2016b)
24P73	23.88	0.27	van Weeren et al. (2011b)

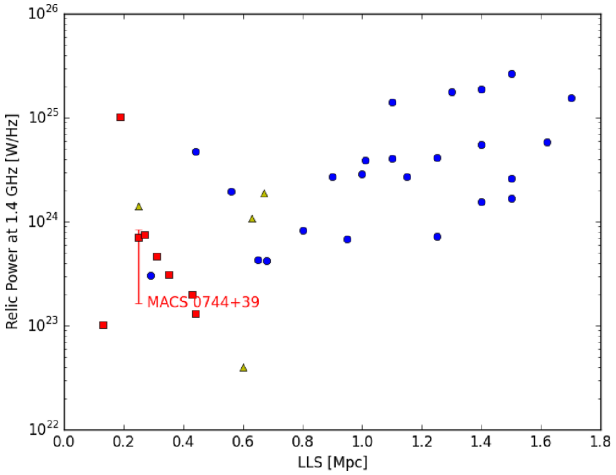

Figure 6. A sample of gischt radio relics (blue circles) and AGN/phoenix relics (red squares) from Nuza et al. (2017) plotted by their power at 1.4 GHz versus their LLS in Mpc. Yellow triangles represent additional relics/candidate relics from Table 1. The red line represents the upper limit range of the power for the radio emission detected within the shocked region for MACS J0744.9+3927. Powers include a *k*-correction to account for redshift, with an average spectral index of $\alpha = -1.2$, as is used in Nuza et al. (2017).

by MUSTANG (250 kpc). The largest value of this power range is fainter than that of most observed gischt-type relics (shown as blue circles in Fig. 6); however, since the LLS is smaller than most gischt-type relics, a lower power would be expected. On the basis of the measured power range alone, a gischt-type relic cannot be ruled out. The power range and LLS agree more closely with powers and sizes seen in phoenix-type relics (shown as red squares in Fig. 6).

Based on the location of the shock and the LLS, it does not seem likely that a gischt-type relic would be generated, and indeed we see no such clear radio structure resembling a gischt relic at the shock site. The absence of a morphological structure resembling a relic is interesting, particularly in light of the high electron acceleration efficiency observed in radio relics, which is still poorly understood (Vazza & Brüggen 2014).

3.3 Upper limit on particle acceleration efficiency

Taking the parameters of the shock wave detected in MACS J0744.9+3927 (an average Mach number of $\mathcal{M} = 1.75$ and shock velocity $V_{\rm sh} = 1827\,{\rm km\,s^{-1}}$) and the non-detection of a radio relic, we can compute an upper limit on the particle acceleration efficiency. Comparing the dissipated kinetic power at the shock to the total power in the radio emission, we can estimate the acceleration efficiency using equation 2 in Botteon et al. (2016a):

$$\int_{\nu_0} L(\nu){\rm d}\nu \simeq \frac{1}{2}\eta_{\rm e}\Psi\rho_{\rm u}V_{\rm sh}^3(1-C^{-2})\frac{B^2}{B_{\rm cmb}^2+B^2}S, \quad (1)$$

where $\eta_{\rm e}$ is the acceleration efficiency, $\rho_{\rm u}$ is the upstream density, $V_{\rm sh}$ is the shock velocity, C is the compression factor that is related to the Mach number via $C = 4\mathcal{M}^2/(\mathcal{M}^2+3)$, B is the magnetic field strength and $B_{\rm cmb} = 3.25(1+z)^2$, S is the surface area of the shock,[11] and Ψ is the ratio of the energy injected in electrons emitting over the full spectrum versus electrons emitting in radio wavelengths, given by

$$\Psi = \frac{\int_{p_0} Q(p)E(p){\rm d}p}{\int_{p_{\rm min}} Q(p)E(p){\rm d}p}, \quad (2)$$

where $Q(p) \propto p^{-\delta_{\rm inj}}$ and $\delta_{\rm inj} = 2(\mathcal{M}^2+1)/(\mathcal{M}^2-1)$ (Blandford & Eichler 1987). The momentum, p_0, is the momentum associated with electrons that emit the characteristic frequency of the synchrotron emission, $\nu_0 = p_0^2 eB/2\pi m_{\rm e}^3c^3$. Here, $m_{\rm e}$ is the electron mass, e its charge, and c the speed of light. For the minimum momentum in the denominator, $p_{\rm min}$, we consider two cases: (1) for a low value of $p_{\rm min} = 0.1 m_{\rm e}c$, the efficiency has to be unrealistically high, $\gg 100$ per cent, and we cannot infer an upper bound for $\eta_{\rm e}$, or (2) the shock re-accelerates a population of relativistic seed electrons with $p_{\rm min} = 100 m_{\rm e}c$, in which case the efficiency must be ≤ 19 per cent since a relic is not observed. Clearly, this number is uncertain, since it depends not only on $p_{\rm min}$, but also quite strongly on the assumed velocity of the shock, $V_{\rm sh}$, the upstream density, $\rho_{\rm u}$, as well as the magnetic field, B. We used the value from fig. 5 in Korngut et al. (2011) for the upstream density ($\rho_{\rm u} = 0.013\,{\rm cm^{-3}}$), and since the magnetic field in this cluster is not known, we assume a value of $B = 1\,\mu$G.

3.4 Missing radio halo

The study of radio haloes in high-mass and high-z merging clusters is crucial to constrain the model of turbulent re-acceleration. In the turbulent re-acceleration scenario, it is expected that the fraction of

[11] This area is the largest linear length times the largest linear width of the shocked region, defined by the pie cut in Fig. 5 ($250 \times 140\,{\rm kpc^2}$).

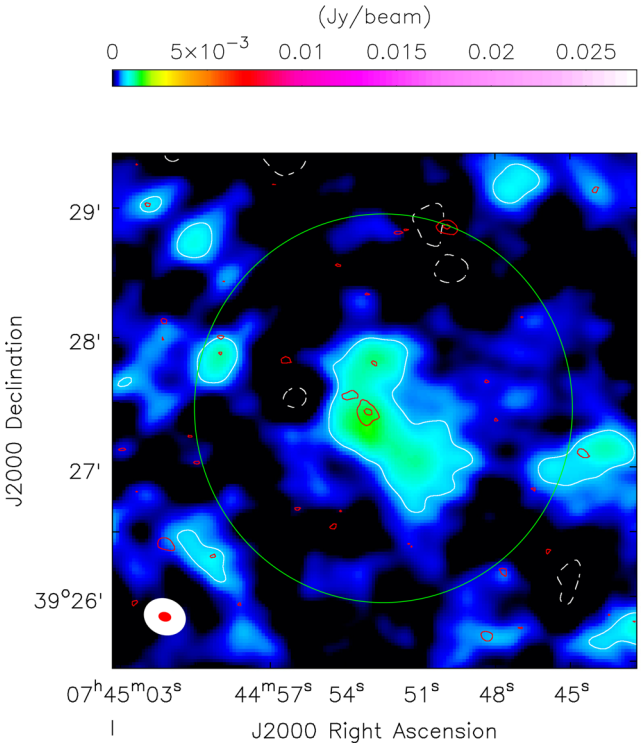

Figure 7. LOFAR image after subtracting sources imaged at a uv-range of $> 4000\ \lambda$. An outer uv-taper of 10 arcsec was used to bring out diffuse emission. rms noise is $\sigma = 200\ \mu$Jy beam^{-1}. White contours represent $[-3, 3] \times \sigma$. Red contours $[3, 12] \times \sigma$ are the compact sources imaged with uv-range $> 4000\ \lambda$, which were subtracted. The green circle represents the area that would be expected for a radio halo in a cluster of this mass, with a radius of 650 kpc. We use flux density measurements in this region to determine the radio halo power upper limit.

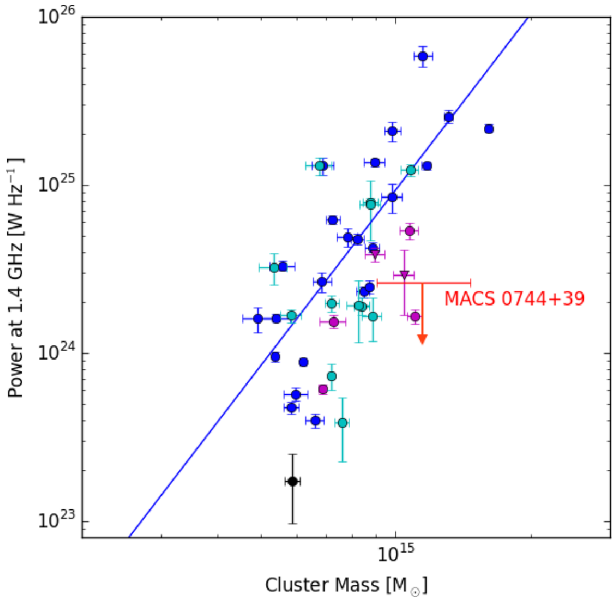

Figure 8. A sample of radio haloes plotted by their radio power at 1.4 GHz versus their cluster mass (M_{500} – as determined from *Planck* observations). The sample of haloes and their correlation are reproduced from Martinez Aviles et al. (2016). Haloes with flux measured at 1.4 GHz are marked by blue circles and their derived fit is shown as a blue line. Cyan circles represent haloes with flux measured at frequencies other than 1.4 GHz. Magenta circles represent ultra-steep haloes, and magenta triangles represent ultra-steep haloes with flux measured at frequencies other than 1.4 GHz. The ultra-steep-spectrum radio halo in Abell 1132 is also included from Wilber et al. (2018), and is marked by a black circle. The upper limit of radio halo power at 1.4 GHz in MACS J0744.9+3927 is represented by the red arrow. We note that this power is likely an overestimation since it consists of AGN lobe power. All the halo powers include a k-correction with an averaged spectral index of $\alpha = -1.3$, as in Martinez Aviles et al. (2016).

ultra-steep-spectrum radio haloes increases strongly with redshift because of stronger inverse Compton losses (Cassano et al. 2010).

In MACS J0744.9+3927, the LOFAR image does not show a radio halo, even though the X-ray and SZ data indicate that this system is in the process of a merger, albeit not a major one. Diffuse emission at the cluster centre is most likely caused by the active BCG as well as the galaxy north of it whose redshift is unknown. If there is radio halo emission, it is eclipsed by the emission of the active galaxies, whose lobes extend to ∼570 kpc. However, a high-mass cluster such as this would be expected to host a radio halo on larger scales (Cassano et al. 2007).

To determine an upper limit on the flux of a radio halo, we use an image made after subtracting compact sources imaged at a uv-range of $> 4000\ \lambda$ (corresponding to emission spanning less than ∼400 kpc) with rms noise of $\sigma = 200\ \mu$Jy beam^{-1} (see Fig. 7). We estimate the upper limit of a radio halo by defining a circular region (shown as the green circle in Fig. 7) with an origin at the cluster centre and a radius of 650 kpc, as would be expected for a cluster of this mass. The upper limit on the flux density is expressed as the summation of flux density from two regions within this circle: (1) the flux density within 3σ contours of the central diffuse emission (which includes AGN emission), and (2) the rms noise, σ, times the number of beams covering the remaining area inside the circle and outside the central 3σ contours. We state that this upper limit of $S_{143} = 19.9$ mJy is probably an overestimate since it clearly includes emission originating from AGN. Assuming a spectral index of $\alpha = -1.3$ and including k-correction, we find that the extrapolated power at 1.4 GHz of this upper limit is $P_{1.4} = 2.61 \times 10^{24}$ W Hz^{-1} and falls below the correlation for radio halo power versus cluster mass for a sample of clusters (see Fig. 8). Since there are no *Planck* observations of this cluster, we must use the cluster mass as derived by weak lensing from CLASH.[12] Given the large errors in the mass for MACS J0744.9+3927, the upper limit for the radio power shown in Fig. 8 is not far from the correlation at the lower end of the mass estimate. Moreover, for a given mass, the scatter in radio halo power is quite large, and the correlation may change once deeper and more systematic searches for haloes are underway.

3.5 Radio halo injection

We simulate a radio halo by injecting a radio source into the uv-data that has a central brightness I_0 and an e-folding radius of r_e, which is defined as the radius at which the brightness drops to I_0/e (e.g. Brunetti et al. 2007; Venturi et al. 2008; Bonafede et al. 2017). The length-scale r_e is therefore relatively independent of the sensitivity of the radio images. The radio halo we inject has a size and brightness specified by the correlation in Fig. 8

[12] The CLASH mass range is consistent within 1σ with the cluster mass value derived from *XMM–Newton* X-ray data.

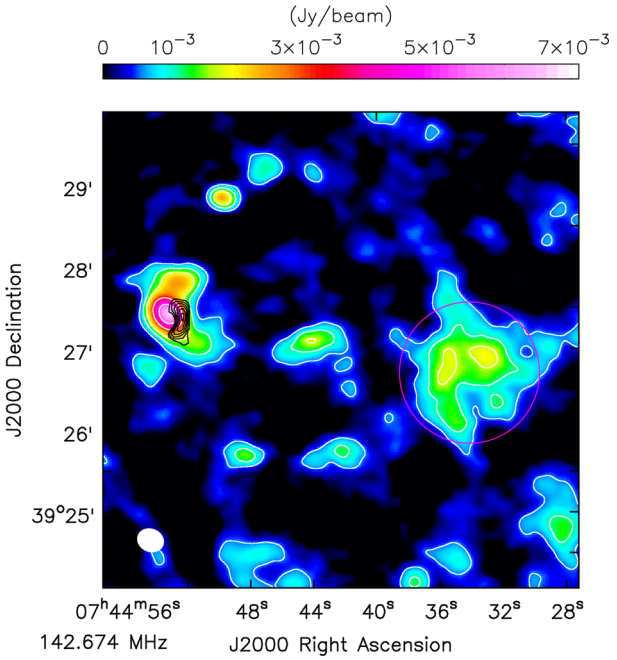

Figure 9. LOFAR image after injecting a simulated radio halo, with a power of $P_{1.4} = 8.54 \times 10^{24}$ W Hz^{-1} at 1.4 GHz and a spectral index of $\alpha = -1.5$, to the west of the cluster centre. The magenta circle has a radius of $3r_e$ centred on the coordinates where the simulated halo was injected. White contours are [2, 4, 6, 12, 18] $\times\ \sigma$, where $\sigma = 300$ μJy beam^{-1}. The flux density of the recovered halo is measured within the circular magenta region, above 2σ, and is found to be 20.02 ± 2.00 mJy.

($P_{1.4} = 8.54 \times 10^{24}$ W Hz^{-1} and $R_H = 650$ kpc for a cluster with $M_{500} = 9.9 \times 10^{14}\,M_\odot$), such that $I_0 = 0.115$ μJy arcsec^2 and $r_e = 250$ kpc. The model of this mock radio halo is Fourier transformed into the visibility data (MODEL_DATA column), taking into account the *w*-projection parameter. A relatively empty region near the cluster centre, void of bright sources or artefacts, is chosen to host the injected flux (at RA: 07^{h}44^{m}34^s.12, Dec.: +39°26′42″.3). The data set is then re-imaged with Briggs' robust parameter 0 and an outer *uv*-taper of 10 arcsec. Since we set the power at 1.4 GHz, a flatter spectral index would translate to a weaker power at 143 MHz than a steeper spectral index.[13] We adjust the spectral index from $\alpha = -1.0$ to -1.8 and determine when the injected flux is visible at 143 MHz. The injected halo is considered detected when it is recovered above 2σ with a diameter of roughly $3r_e$. We find that the spectral index must be $\alpha \leq -1.5$ for the halo to be recovered in our LOFAR images. With a spectral index of $\alpha = -1.5$, the total integrated flux density of the injected halo is 26.6 mJy at 143 MHz. Our LOFAR image of this simulated halo is shown in Fig. 9.

The flux density of the recovered halo is then measured in our LOFAR image within a region centred on the coordinates of the injected halo with a diameter of roughly $3r_e$. The integrated flux density of the recovered halo, above 2σ, is found to be 20.02 ± 2.00 mJy. This observed flux density is 75 per cent that of the injected flux density. Compared to our upper limit determined in Section 3.4, the recovered flux density of the mock halo is approximately equal. If a halo with a spectral index ≤ -1.5 was present in this cluster, it is likely that our flux density upper limit would have been greater than the flux density of the recovered mock halo since our upper limit was measured including AGN emission as well. We argue that a halo with spectral index ≤ -1.5 is not present in this cluster, and that a halo with a flatter spectral index may exist but cannot be detected by our LOFAR observations at 143 MHz.

[13] Radio haloes are usually shown to exhibit spectral indices < -1.

4 DISCUSSION AND CONCLUSION

SZ and X-ray observations have revealed a shock, with Mach number $\mathcal{M} = 1.0$–2.9 and a length of ∼200 kpc, near the centre of the cluster MACS J0744.9+3927. To search for diffuse radio emission associated with the merger, we have imaged the cluster with LOFAR at 120–165 MHz. Our LOFAR radio images do not show a radio relic coincident with the shock nor the presence of a radio halo at the cluster centre. With its estimated Mach number close to the Mach numbers of giant shock waves observed on cluster outskirts (which form powerful radio relics such as the Toothbrush relic), a search for radio emission associated with the shock in MACS J0744.9+3927 is important to understand the mechanisms of particle acceleration in the ICM.

Although the shock detected by MUSTANG is considered to be merger induced by Korngut et al. (2011), it is very different from shocks that produce gischt-type relics, which are typically found on the cluster outskirts, since it is smaller and near the cluster centre. Instead of being induced by a merger, the shock may have been caused by an outburst of the central AGN. However, in Korngut et al. (2011), it is also reported that there is the presence of a cold front behind the shock; this lends support to the merger-induced scenario for the shock front. Interestingly, simulations show bright mock relics occurring close to the cluster centre (Nuza et al. 2017); however, these have not yet been confirmed by observations.

The upper limit of the radio luminosity in the shocked region also suggests that no DSA at the shock front takes place as this process generally leads to higher luminosities relative to the size of the source (see Fig. 6). It is unclear why no DSA takes place, at least not with the efficiency that is observed in large radio relics. The magnetic field direction may have an influence on the efficiency of electron acceleration (e.g. Guo et al. 2014b). However, Wittor et al. (2017) have shown that the magnetic field distributions in galaxy clusters as predicted by cosmological magnetohydrodynamical simulations have little effect on the radio luminosities of radio relics.

If pre-existing populations of older cosmic ray (CR) electrons are required for the injection into a DSA process, one would expect that close to a central radio galaxy there should be no shortage of seed CR electrons: a phoenix-type relic caused by the re-acceleration of old AGN lobes might be expected in MACS J0744.9+3927. The AGN should contribute mildly energetic electrons, which could then be re-accelerated via compression by the shock front. Another recently proposed mechanism is 'gentle re-energization' (de Gasperin et al. 2017), in which old CR electrons get accelerated on time-scales larger than sound crossing times to produce steep and filamentary radio emission, but this does not appear to happen in MACS J0744.9+3927.

While we suggest that the radio flux within the shocked region is probably not attributed to a gischt-type relic, due to the small size and central location of the shock, deeper upper limits on the radio power would be required to rule out this possibility. The upper limit of the radio power and the LLS of the shocked region agree more closely to known phoenix/AGN relics, but we argue that the emission present is not actually re-energized relic emission but simply a contamination from the original AGN lobe emission of the BCG.

Since we do not see a relic, or a re-brightening of AGN emission (in the form of a phoenix), it could be the case that the shock and the AGN are not in the same plane and that there is not a sufficient supply of seed electrons being injected into the shocked region. We find that the energy dissipated at the shock would be insufficient to accelerate a population of only very mildly relativistic electrons ($p_{\rm min} = 0.1 m_{\rm e} c$).

There is some disparity between the Mach numbers as determined from X-ray observations versus radio observations. It has been shown that radio emission of relics traces higher Mach numbers than those inferred from temperature or brightness discontinuities in X-ray (Hong, Kang & Ryu 2015; Itahana et al. 2015; Trasatti et al. 2015; Akamatsu et al. 2017). However, a Mach number of $\mathcal{M} = 2.1^{+0.8}_{-0.5}$ as inferred from MUSTANG and *Chandra* data is comparable to Mach numbers found, e.g., in the Toothbrush relic.

Finally, we also see no signs of a giant radio halo despite that this cluster is massive ($M_{500} = (11.837 \pm 2.786) \times 10^{14}\,{\rm M}_{\odot}$; Sereno et al. 2015) and considered to be a merger. Radio haloes at high redshifts are expected to have shorter lifetimes because of the higher inverse Compton losses. Hence, one would expect a higher fraction of ultra-steep-spectrum haloes compared to lower redshifts. Still, the El Gordo cluster, which is one of the highest redshift ($z = 0.9$) and most massive merging clusters known, exhibits, both, radio relics and a radio halo that can be seen over a range of radio frequencies. Since MACS J0744.9+3927 has a mass similar to that of the El Gordo cluster, and is at a slightly lower redshift, it is surprising that a radio halo is not visible at low radio frequencies.

A simulation of a radio halo injected into our LOFAR data proves that a halo falling on the correlation line for a cluster of this mass, with a spectral index $\alpha \leq -1.5$, is not present in the cluster. This cluster may host a radio halo with a flatter spectrum to which our low-frequency observations are not sensitive. This also brings into question the merger phase of this cluster. If it is in an early phase, it may explain why the merger shock is small and so close to the cluster centre, and also why a radio halo with steep-spectrum emission is not yet visible.

ACKNOWLEDGEMENTS

This work was supported by the Deutsche Forschungsgemeinschaft (DFG) through the Collaborative Research Centre SFB 676 'Particles, Strings and the Early Universe', project C2. LOFAR, the Low Frequency Array designed and constructed by ASTRON, has facilities in several countries, which are owned by various parties (each with their own funding sources) and which are collectively operated by the International LOFAR Telescope (ILT) foundation under a joint scientific policy. The LOFAR software and dedicated reduction packages on https://github.com/apmechev/GRID_LRT were deployed on the e-infrastructure by the LOFAR e-infragroup, consisting of J. B. R. Oonk (ASTRON and Leiden Observatory), A. P. Mechev (Leiden Observatory), and T. Shimwell (Leiden Observatory) with support from N. Danezi (SURFsara) and C. Schrijvers (SURFsara). This work has made use of the Dutch national e-infrastructure with the support of SURF Cooperative through grant e-infra160022. This work has also made use of the Lofar Solution Tool (LoSoTo), developed by F. de Gasperin. This research has made use of the NASA/IPAC Extragalactic Database (NED), which is operated by the JPL, California Institute of Technology under contract with the National Aeronautics and Space Administration. A. Bonafede acknowledges supports from the ERC Stg 714245 DRANOEL. RvW acknowledges support from the ERC Advanced Investigator programme NewClusters 321271. DW acknowledges support by the DFG through grants SFB 676 and BR 2026/17 and by the ERC through Project No. 714196. We acknowledge Felipe Andrade-Santos for his helpful comments.

REFERENCES

Akamatsu H. et al., 2017, A&A, 600, A100
Bagchi J., Durret F., Neto G. B. L., Paul S., 2006, Science, 314, 791
Basu K., Sommer M., Erler J., Eckert D., Vazza F., Magnelli B., Bertoldi F., Tozzi P., 2016, ApJ, 829, L23
Blandford R., Eichler D., 1987, Phys. Rep., 154, 1
Blandford R. D., Ostriker J. P., 1978, ApJ, 221, L29
Böhringer H. et al., 2000, ApJS, 129, 435
Bonafede A., Giovannini G., Feretti L., Govoni F., Murgia M., 2009, A&A, 494, 429
Bonafede A., Intema H. T., Brüggen M., Girardi M., Nonino M., Kantharia N., van Weeren R. J., Röttgering H. J. A., 2014, ApJ, 785, 1
Bonafede A. et al., 2017, MNRAS, 470, 3465
Botteon A., Gastaldello F., Brunetti G., Dallacasa D., 2016a, MNRAS, 460, L84
Botteon A., Gastaldello F., Brunetti G., Kale R., 2016b, MNRAS, 463, 1534
Botteon A., Gastaldello F., Brunetti G., 2018, MNRAS, 00, 00
Brüggen M., van Weeren R. J., Röttgering H. J. A., 2011, Mem. Soc. Astron. Ital., 82, 627
Brüggen M., Bykov A., Ryu D., Röttgering H., 2012, Space Sci. Rev., 166, 187
Brunetti G., Jones T. W., 2014, Int. J. Mod. Phys. D, 23, 1430007
Brunetti G., Setti G., Feretti L., Giovannini G., 2001, MNRAS, 320, 365
Brunetti G., Venturi T., Dallacasa D., Cassano R., Dolag K., Giacintucci S., Setti G., 2007, ApJ, 670, L5
Cassano R., Brunetti G., Setti G., Govoni F., Dolag K., 2007, MNRAS, 378, 1565
Cassano R., Brunetti G., Röttgering H. J. A., Brüggen M., 2010, A&A, 509, A68
Cohen A. S., Clarke T. E., 2011, AJ, 141, 149
Condon J. J., Cotton W. D., Greisen E. W., Yin Q. F., Perley R. A., Taylor G. B., Broderick J. J., 1998, AJ, 115, 1693
de Gasperin F., Ogrean G. A., van Weeren R. J., Dawson W. A., Brüggen M., Bonafede A., Simionescu A., 2015, MNRAS, 448, 2197
de Gasperin F. et al., 2017, Sci. Adv., 3, e1701634
Durret F. et al., 2016, A&A, 588, A69
Ebeling H., Barrett E., Donovan D., Ma C.-J., Edge A. C., van Speybroeck L., 2007, ApJ, 661, L33
Eckert D., Jauzac M., Vazza F., Owers M. S., Kneib J.-P., Tchernin C., Intema H., Knowles K., 2016, MNRAS, 461, 1302
Ensslin T. A., Biermann P. L., Klein U., Kohle S., 1998, A&A, 332, 395
Enßlin T. A. Gopal-Krishna, 2001, A&A, 366, 26
Erler J., Basu K., Trasatti M., Klein U., Bertoldi F., 2015, MNRAS, 447, 2497
Feretti L., Giovannini G., Govoni F., Murgia M., 2012, A&ARv, 20, 54
Ferrari C. et al., 2011, A&A, 534, L12
Guennou L. et al., 2014, A&A, 561, A112
Guo X., Sironi L., Narayan R., 2014a, ApJ, 794, 153
Guo X., Sironi L., Narayan R., 2014b, ApJ, 797, 47
Hales S. E. G., Riley J. M., Waldram E. M., Warner P. J., Baldwin J. E., 2007, MNRAS, 382, 1639
Hlavacek-Larrondo J. et al., 2018, MNRAS, 475, 2743
Hoang D. N. et al., 2017, MNRAS, 471, 1107
Hoeft M., Brüggen M., 2007, MNRAS, 375, 77
Hong S. E., Kang H., Ryu D., 2015, ApJ, 812, 49
Intema H. T., Jagannathan P., Mooley K. P., Frail D. A., 2017, A&A, 598, A78
Itahana M., Takizawa M., Akamatsu H., Ohashi T., Ishisaki Y., Kawahara H., van Weeren R. J., 2015, PASJ, 67, 113
Kempner J. C., Sarazin C. L., 2001, ApJ, 548, 639
Kitayama T., Komatsu E., Ota N., Kuwabara T., Suto Y., Yoshikawa K., Hattori M., Matsuo H., 2004, PASJ, 56, 17

Komatsu E. et al., 2001, PASJ, 53, 57
Korngut P. M. et al., 2011, ApJ, 734, 10
McMullin J. P., Waters B., Schiebel D., Young W., Golap K., 2007, in Shaw R. A., Hill F., Bell D. J., eds, ASP Conf. Ser. Vol. 376, Astronomical Data Analysis Software and Systems XVI. Astron. Soc. Pac., San Francisco, p. 127
Markevitch M., Vikhlinin A., 2007, Phys. Rep., 443, 1
Markevitch M., Gonzalez A. H., David L., Vikhlinin A., Murray S., Forman W., Jones C., Tucker W., 2002, ApJ, 567, L27
Markevitch M., Govoni F., Brunetti G., Jerius D., 2005, ApJ, 627, 733
Martinez Aviles G. et al., 2016, A&A, 595, A116
Mason B. S. et al., 2010, ApJ, 716, 739
Matsukiyo S., Ohira Y., Yamazaki R., Umeda T., 2011, ApJ, 742, 47
Nuza S. E., Gelszinnis J., Hoeft M., Yepes G., 2017, MNRAS, 470, 240
Offringa A. R. et al., 2014, MNRAS, 444, 606
Ogrean G. A., Brüggen M., Röttgering H., Simionescu A., Croston J. H., van Weeren R., Hoeft M., 2013, MNRAS, 429, 2617
Postman M. et al., 2012, ApJS, 199, 25
Richard J., Jones T., Ellis R., Stark D. P., Livermore R., Swinbank M., 2011, MNRAS, 413, 643
Romero C. E. et al., 2015, ApJ, 807, 121
Rottgering H. J. A., Wieringa M. H., Hunstead R. W., Ekers R. D., 1997, MNRAS, 290, 577
Russell H. R., Sanders J. S., Fabian A. C., Baum S. A., Donahue M., Edge A. C., McNamara B. R., O'Dea C. P., 2010, MNRAS, 406, 1721
Russell H. R. et al., 2011, MNRAS, 417, L1
Scaife A. M. M., Heald G. H., 2012, MNRAS, 423, L30
Sereno M., Giocoli C., Ettori S., Moscardini L., 2015, MNRAS, 449, 2024
Shimwell T. W., Brown S., Feain I. J., Feretti L., Gaensler B. M., Lage C., 2014, MNRAS, 440, 2901
Shimwell T. W. et al., 2016, MNRAS, 459, 277
Shimwell T. W. et al., 2017, A&A, 598, A104
Slee O. B., Roy A. L., Murgia M., Andernach H., Ehle M., 2001, AJ, 122, 1172
Trasatti M., Akamatsu H., Lovisari L., Klein U., Bonafede A., Brüggen M., Dallacasa D., Clarke T., 2015, A&A, 575, A45
Uchida Y., Simionescu A., Takahashi T., Werner N., Ichinohe Y., Allen S. W., Urban O., Matsushita K., 2016, PASJ, 68, S20
van Haarlem M. P. et al., 2013, A&A, 556, A2
van Weeren R. J., Röttgering H. J. A., Brüggen M., Hoeft M., 2010, Science, 330, 347
van Weeren R. J., Röttgering H. J. A., Brüggen M., 2011a, A&A, 527, A114
van Weeren R. J., Hoeft M., Röttgering H. J. A., Brüggen M., Intema H. T., van Velzen S., 2011b, A&A, 528, A38
van Weeren R. J., Röttgering H. J. A., Intema H. T., Rudnick L., Brüggen M., Hoeft M., Oonk J. B. R., 2012, A&A, 546, A124
van Weeren R. J. et al., 2016a, ApJS, 223, 2
van Weeren R. J. et al., 2016b, ApJ, 818, 204
van Weeren R. J. et al., 2017, Nat. Astron., 1, 0005
Vazza F., Brüggen M., 2014, MNRAS, 437, 2291
Vazza F., Brunetti G., Gheller C., 2009, MNRAS, 395, 1333
Vazza F., Brüggen M., Wittor D., Gheller C., Eckert D., Stubbe M., 2016, MNRAS, 459, 70
Vazza F., Jones T. W., Brüggen M., Brunetti G., Gheller C., Porter D., Ryu D., 2017, MNRAS, 464, 210
Venturi T., Giacintucci S., Dallacasa D., Cassano R., Brunetti G., Bardelli S., Setti G., 2008, A&A, 484, 327
White R. L., Becker R. H., Helfand D. J., Gregg M. D., 1997, ApJ, 475, 479
Wilber A. et al., 2018, MNRAS, 473, 3536
Williams W. L. et al., 2016, MNRAS, 460, 2385
Wittor D., Vazza F., Brüggen M., 2017, MNRAS, 464, 4448
Young A. H. et al., 2015, ApJ, 809, 185

This paper has been typeset from a TEX/LATEX file prepared by the author.